EVOLUTION OF THE RADIUS VALLEY AROUND LOW MASS DWARF STARS WITH *KEPLER* AND *K2*

Ryan Cloutier[1,2] et al.
Draft version October 17, 2019

ABSTRACT

Recent observational studies have revealed a prominent gap in the occurrence rate of close-in planet radii around Sun-like stars. Resolving the so-called radius valley around low mass stars can provide valuable constraints on the physical mechanisms that sculpt the valley and so far have been largely limited by relatively poor counting statistics. Here we calculate the occurrence rate of small close-in planets around low mass dwarf stars using the known planet populations from both the primary *Kepler* and *K2* missions while exploiting the precise *Gaia* DR2 data to refine the stellar radii and masses. After applying appropriate completeness corrections to the empirical planet populations, the radius valley is clearly resolved in the maximum a-posteriori occurrence rates although the gap is not completely void of planets, a feature whose prominence increases with decreasing stellar mass. We also show that the location of valley features evolve to smaller planet sizes with decreasing stellar mass in agreement with competing models of photoevaporation and core-powered mass loss. Although current measurements are insufficient to firmly distinguish either model as the dominant formation pathway of the radius valley, we argue that robust inferences will require $\mathcal{O}(?)$ additional confirmed close-in planets around low mass stars which are expected to be uncovered by *TESS* within its extended mission.

1. INTRODUCTION

NASA's *Kepler* space telescope has discovered thousands of exoplanets over its lifetime and consequently enabled robust investigations of the occurrence rate of planets within our galaxy. One striking outcome of such studies was that the so-called super-Earths and sub-Neptunes—whose radii span sizes intermediate between those of the Earth and Neptune—represent the most common type of planet around Sun-like stars and early M dwarfs alike (e.g. Youdin 2011; Howard et al. 2012; Dressing & Charbonneau 2013; Fressin et al. 2013; Petigura et al. 2013; Morton & Swift 2014; Dressing & Charbonneau 2015; Gaidos et al. 2016; Fulton et al. 2017; Hardegree-Ullman et al. 2019). Furthermore, mass measurements of many of these transiting planets via transit-timing variations or precision radial velocity measurements revealed that the majority of planets smaller than $\sim 1.6\ \mathrm{R_\oplus}$ are consistent with having bulk terrestrial compositions (e.g. Weiss & Marcy 2014; Dressing et al. 2015; Rogers 2015).

Early studies of the *Kepler* planet population hinted that planets at small orbital separations exhibited a bimodal radius distribution (e.g. Owen & Wu 2013)—commonly referred to as the radius valley—that is thought to depict a population of small, predominantly rocky super-Earths plus a population of inflated sub-Neptunes that have retained significant H/He envelopes. Consequently, numerous studies of planet formation and evolution sought to explain this apparent bimodality. One such proposed mechanism is that of photoevaporation wherein the gaseous envelopes of small close-in planets may be stripped by X-ray and extreme ultraviolet (XUV) radiation from their host stars during the first

cloutier@cfa.harvard.edu
[1] Center for Astrophysics | Harvard & Smithsonian, 60 Garden Street, Cambridge, MA, 02138, USA
[2] Dept. of Astronomy & Astrophysics, University of Toronto, 50 St. George Street, Toronto, ON, M5S 3H4, Canada

~ 100 Myrs of the planet's lifetime (Owen & Wu 2013; Jin et al. 2014; Lopez & Fortney 2014; Chen & Rogers 2016; Owen & Wu 2017; Jin & Mordasini 2018; Lopez & Rice 2018). Another possible explanation invokes gas-poor formation wherein gas accretion is delayed by dynamical friction whilst the planetary core is still embedded within the protoplanetary disk until a point at which the gaseous disk has almost completely dissipated after just a few Myrs (Lee et al. 2014; Lee & Chiang 2016; Lopez & Rice 2018). More recently, the radius valley may also be explained by core-powered mass loss wherein the luminosity from a planetary core's primordial energy reservoir from formation drives atmospheric escape over Gyr timescales (Ginzburg et al. 2018; Gupta & Schlichting 2019a,b).

Observational tests of the aforementioned theoretical frameworks have become feasible in recent years due to the precise refinement of measured planet radii following improved stellar host characterization via spectroscopy, asteroseismology, and *Gaia* parallaxes (e.g. Fulton et al. 2017; Berger et al. 2018; Fulton & Petigura 2018; Van Eylen et al. 2018; Martinez et al. 2019). These studies clearly resolved the radius valley among small close-in planets around Sun-like stars. A variety of trends were also observed in either the raw or in the completeness-corrected (i.e. the occurrence rate) distributions of close-in planets. Firstly, the location of the radius valley around FGK stars is period-dependent with slope $\mathrm{d}\log r_p/\mathrm{d}\log P \sim -0.1$ (Van Eylen et al. 2018; Martinez et al. 2019), a result that is consistent with both photoevaporation and core-powered mass loss models but is inconsistent with the late formation of terrestrial planets in a gas-poor environment. Secondly, the feature locations (i.e. the weighted average radius of the peaks and valley) appear to exist at smaller planet radii with decreasing stellar mass (Fulton & Petigura 2018; Wu 2019).

In this study, we extend the investigation of the occurrence rate of close-in planets to systems hosted by

FIG. 1.— Empirical distributions of *Kepler* planet radii. Histograms of *Kepler* planet radii from Berger et al. (2018) for planets with host stellar effective temperatures $T_{\rm eff} \in [4700, 6500]$ K (*blue*) and $T_{\rm eff} < 4700$ K (*red*). The former subset of 2816 planets corresponds to the effective temperature range considered in the CKS (Fulton et al. 2017) wherein the radius valley is clearly resolved in the empirical distribution even without completeness corrections. A similar bimodal structure is not resolved in the empirical distribution of the latter subset around cool stars due in-part to the relatively poor counting statistics with just 350 planets.

low mass dwarf stars later than mid-K dwarfs. The known planet population in this stellar mass regime features nearly an order of magnitude fewer planets than around Sun-like stars, thus making the detection of the radius valley around low mass stars more difficult and at a lower signal-to-noise. This fact is clearly evidenced in the empirical *Kepler* planet population for which the radius valley around Sun-like stars ($T_{\rm eff} \in [4700, 6500]$ K) is clearly exhibited whereas a similar feature around low mass stars ($T_{\rm eff} < 4700$ K) is not easily discernible by-eye (see Fig. 1 based on the data from Berger et al. 2018). Our study leverages the precise stellar parallaxes from the *Gaia* DR2 for low mass stars observed by *Kepler* and *K2* to refine the stellar parameters and compute precise occurrence rates of close-in planets with the goal of resolving the radius valley and accurately measuring the locations of the radius valley features and their uncertainties. Although it is unlikely that a single physical mechanism is responsible for sculpting the radius valley, investigation the evolution of the valley features with stellar mass can allude to which process—if any—dominates the evolution of close-in planets.

In Sects. 2 and 3 we define our stellar sample from *Kepler* and *K2* and compile our sample of confirmed planets for each mission. In Sect. 4 we derive the transiting planet detection completeness and use those results to calculate the occurrence rate of small close-in planets and resolve the radius valley in Sect. 5. Our results as a function stellar mass are compared to model predictions in Sect. 6 and we conclude with a discussion of our results and its implications in Sect. 7.

2. LOW MASS DWARF STELLAR SAMPLE

The goal of this study is to extend measurements of the radius valley and its properties to planetary systems hosted by low mass dwarf stars with effective temperatures $T_{\rm eff} < 4700$ K: the lower limit of $T_{\rm eff}$ considered by Fulton & Petigura (2018). This adopted temperature threshold approximately corresponds to spectral types later than K3.5V (Pecaut & Mamajek 2013). In the following subsections we define our stellar sample from both *Kepler* or *K2*.

2.1. *Kepler Stellar Sample*

Following the release of *Gaia* DR2 (Lindegren et al. 2018), Berger et al. (2018) cross-matched *Kepler* target stars with DR2 and compiled a catalog of stellar parallaxes ϖ, 2MASS K_s-band magnitudes, and spectroscopic measurements of $T_{\rm eff}$, $\log g$, and [Fe/H] for $\sim 178,000$ stars observed as part of the primary *Kepler* mission. Spectroscopic measurements were obtained from either the DR25 Kepler Stellar Properties Catalog (KSPC; Mathur et al. 2017), the California Kepler Survey (CKS; Petigura et al. 2017) where available, and $T_{\rm eff}$ values for stars with $T_{\rm eff} < 4000$ K were compiled from

Gaidos et al. (2016). The full set of available stellar parameters are used as input within the spectral classification code `isoclassify` (Huber et al. 2017) to calculate stellar luminosities. The resulting luminosity values were consequently combined with the $T_{\rm eff}$ measurements to refine the stellar radii using the Stefan-Boltzmann law for the majority of *Kepler* FGK stars. However, bolometric corrections for *Kepler* M dwarfs with $T_{\rm eff} < 4100$ K and absolute K_s-band magnitudes $M_{K_s} > 3$ are known to suffer significant inaccuracies owing to incomplete molecular line lists. For these stars, Berger et al. (2018) instead adopted the empirically-derived M dwarf radius-luminosity relation from Mann et al. (2015) to refine their M dwarf stellar radii. Berger et al. (2018) also used the $T_{\rm eff}$ values and their luminosity measurements to derive stellar evolutionary flags that classify their stars as either a dwarf, a subgiant, or a red giant.

Stellar masses M_s are not reported by Berger et al. (2018). In order to study the *Kepler* planet population as a function of M_s, we derive M_s values given the measured stellar radii R_s using the mass-radius relation from Boyajian et al. (2012) which is applicable to both K and M dwarfs. Boyajian et al. (2012) acquired interferometric measurements with the *CHARA* array of 21 nearby K and M dwarfs to measure the angular size of each stellar disk at the level of $\lesssim 5\%$. Their stellar sample was supplemented by 12 literature measurements of R_s from interferometry. Mass measurements were then derived using the K_s-band mass-luminosity relation from Henry & McCarthy (1993) which was valid for their full stellar sample spanning 0.13-0.90 R$_\odot$. Boyajian et al. (2012) parameterized the stellar mass-radius relationship as a quadratic in M_s and reported values and uncertainties for each polynomial coefficient. Here, we assume independent Gaussian probability density functions (PDF) for each coefficient and sample their values along with each star's R_s from their respective measurement uncertainties to derive the M_s PDF for all of the low mass dwarfs in our *Kepler* sample.

We define our final *Kepler* stellar sample by focusing on stars that satisfy the following criteria:

1. *Kepler* magnitude $K_p < 16$,

2. $T_{\rm eff} - \sigma_{T_{\rm eff}} \leq 4700$ K,

3. $R_s - \sigma_{R_s} \leq 0.8$ R$_\odot$,

4. $M_s - \sigma_{M_s} \leq 0.8$ M$_\odot$, and

5. and an evolutionary flag corresponding to a dwarf star.

Based on these criteria, we retrieve 3965 low mass *Kepler* stars whose stellar parameters are depicted in Fig. 2. In our *Kepler* sample, the *Kepler* magnitudes span $K_p \in [10.35, 16.00]$ with a median value of 15.16, effective temperatures span $T_{\rm eff} \in [3154, 4870]$ K with a median value of 4394 K, stellar radii span $R_s \in [0.17, 0.87]$ R$_\odot$ with a median value of 0.68 R$_\odot$, and stellar masses span $M_s \in [0.13, 0.88]$ M$_\odot$ with a median value of 0.70 M$_\odot$. The stars in this sample exhibit a median fractional R_s uncertainty of $\sim 6.7\%$ which is $\sim 4 - 5$ times smaller than the typical R_s uncertainty reported in the KSPC. The median fractional uncertainty on M_s is $\sim 5.5\%$.

2.2. *K2 Stellar Sample*

We first retrieved the list of probable low mass dwarf stars observed in any *K2* campaign by querying MAST[3]. Our initial search was restricted to *K2* stars with $T_{\rm eff}$ < 4900 K, $\log g$ > 4, and R_s < 1 R$_\odot$. Note that these criteria are not intended to represent the parameter ranges for low mass dwarf stars but are intended as conservative conditions to encapsulate all such stars prior to their refinement based on the *Gaia* DR2 data. From MAST we retrieve each star's Ecliptic Plane Input Catalog (EPIC) numerical identifier, stellar photometry in the *Kepler* bandpass K_p and 2MASS bands JHK_s, along with measured values of $T_{\rm eff}$, $\log g$, [Fe/H], and R_s.

We proceed with refining the stellar parameters by cross-matching our initial *K2* sample with *Gaia* DR2 using the *Gaia-K2* data products from Megan Bedell[4]. Where available, we retrieve reach star's celestial coordinates, stellar parallaxes ϖ, and *Gaia* photometry. Measurements of R_s then follow from the methodology outlined in Berger et al. (2018). The formalism of Bailer-Jones et al. (2018) is used to transform the assumed Gaussian-distributed ϖ PDFs into stellar distance PDFs which need not remain Gaussian. Using the measured distances d and celestial coordinates, we interpolate over the E_{B-V} extinction maps using the mwdust software (Bovy et al. 2016) to derive both the the the V and K_s-band extinction coefficients A_V and A_{K_s}. We then calculate each star's absolute K_s-band magnitude $M_{K_s} = K_s - \mu - A_{K_s}$ where the distance modulus is $\mu = 5 \log_{10}(d/10 \text{ pc})$.

For the earliest stars in our sample ($M_{K_s} \leq 4.6$), for which the bolometric corrections are still reliable, we interpolate the MIST bolometric correction grids (Choi et al. 2016) over $T_{\rm eff}$, $\log g$, [Fe/H], and A_V to derive the K_s-band bolometric corrections BC_{K_s}. We then compute the absolute bolometric magnitude $M_{\rm bol} = M_{K_s} + BC_{K_s}$ and consequently the bolometric stellar luminosities as

$$L_{\rm bol} = L_0 \cdot 10^{-0.4 M_{\rm bol}}, \qquad (1)$$

where $L_0 = 3.0128 \times 10^{28}$ W (Mamajek et al. 2015). The refined R_s values are then calculated using the Stefan-Boltzmann law given $L_{\rm bol}$ and $T_{\rm eff}$ with measurement uncertainties propagated throughout.

For the remaining late type stars with $M_{K_s} > 4.6$, we revert to the empirically-derived radius-luminosity relation from Mann et al. (2015) to calculate the M dwarf stellar radii. Mann et al. (2015) fit a second-order polynomial to R_s as a function of M_{K_s} which has a characteristic dispersion in the fractional radius uncertainty of 2.89%. To quantify the final R_s uncertainty we sample M_{K_s} from its posterior PDF and transform each M_{K_s} draw to an R_s value using the aforementioned radius-luminosity relation. To each star's derived R_s PDF, we add in quadrature an additional dispersion term whose fractional uncertainty is 2.89%. Stellar masses within our *K2* sample are derived identically to the method applied to the *Kepler* sample (see Sect. 2.1) using the Boyajian

et al. (2012) stellar mass-radius relation.

We define our final *K2* stellar sample of low mass dwarf stars similarly to our definition of the *Kepler* sample. Explicitly, we focus on stars that obey the following criteria:

1. $K_p < 14.7$,

2. $T_{\rm eff} - \sigma_{T_{\rm eff}} \leq 4700$ K,

3. $R_s - \sigma_{R_s} \leq 0.8$ R$_\odot$,

4. $M_s - \sigma_{M_s} \leq 0.8$ M$_\odot$, and

5. $R_s < R_{s,\max}$.

Because our *K2* sample lacks any evolutionary flags, we adopt the following ad hoc upper limit on R_s from Fulton et al. (2017) that aims to reject evolved stars:

$$R_{s,\max} = {\rm R}_\odot \cdot 10^{0.00025(T_{\rm eff}/{\rm K}-5500)+0.2}. \qquad (2)$$

Based on these criteria, we retrieve 13428 low mass *K2* stars whose stellar parameters are also depicted in Fig. 2. In our *K2* sample, the *Kepler* magnitudes span $K_p \in [8.47, 14.68]$ with a median value of 14.04, effective temperatures span $T_{\rm eff} \in [3246, 4856]$ K with a median value of 4017 K, stellar radii span $R_s \in [0.14, 0.94]$ R$_\odot$ with a median value of 0.70 R$_\odot$, and stellar masses span $M_s \in [0.09, 0.93]$ M$_\odot$ with a median value of 0.69 M$_\odot$. The stars in this sample exhibit a median fractional R_s uncertainty of $\sim 3.5\%$ which is ~ 2 times smaller than the typical R_s uncertainty obtained for stars in our *Kepler* sample. The median fractional uncertainty on M_s is $\sim 3.9\%$.

3. POPULATION OF SMALL CLOSE-IN PLANETS AROUND LOW MASS DWARF STARS

Here we define the population of small close-in planets orbiting stars contained in our stellar sample. Our initial sample of transiting planets from either *Kepler* or *K2* were retrieved from the NASA Exoplanet Archive (Akeson et al. 2013) on June 15, 2019. Only confirmed planets—based on their Exoplanet Archive dispositions—with orbital periods $P \in [0.5, 100]$ days are included. By considering confirmed planets only we naturally focus on a subset of the true empirical population of small close-in planets without being contaminated by various astrophysical false positive scenarios that may plague the planet candidates that are excluded from our initial sample.

The refined stellar radii derived in Sect. 2 enable us to derive more accurate and precise planetary radii. We refine the planetary radii r_p by retrieving point estimates of each planet's scaled planetary radius r_p/R_s which often include a median value accompanied by the 16$^{\rm th}$ and 84$^{\rm th}$ percentiles. In cases for which the r_p/R_s uncertainties are symmetric, we assume that the r_p/R_s posterior PDF is Gaussian. For planets with asymmetric reported uncertainties, we fit the r_p/R_s percentiles with a skew-normal distribution using the scipy.skewnorm python class. We fit for the location, scale, and shape parameters

of the skew-normal distribution such that its resulting percentiles are consistent with the r_p/R_s point estimates reported for each planet. The refined planetary radii are then derived by sampling the fitted r_p/R_s and R_s distributions. Based on the refined r_p values we update our planet sample by only focusing on planets whose radii are consistent with 0.5-4 $R_\oplus$.

From the distributions of R_s, T_{eff}, M_s, and P or each planet and host star, we derive the planets' semimajor axes a and insolations F via

$$\frac{F}{F_\oplus} = \left(\frac{R_s}{R_\odot}\right)^2 \left(\frac{T_{\text{eff}}}{5777 \text{ K}}\right)^4 \left(\frac{a}{1 \text{ AU}}\right)^{-2}. \quad (3)$$

Our final sample of confirmed small close-in planets contains 275 *Kepler* and 53 *K2* planets respectively. Their respective median fractional radius uncertainties are 7.1% and 9.0%. Planet properties of the 326 confirmed planets in our sample are reported in Tables 1 and 2. Our planet sample is depicted in Fig. 3 as two-dimensional maps of the number of planet detections in the period-radius and insolation-radius spaces. The two-dimensional histogram maps are computed by Monte-Carlo sampling planets from their F and r_p measurement uncertainties and with a fractional precision on P inflated to 20%.

4. TRANSITING PLANET DETECTION COMPLETENESS

Derivation of the planet occurrence rate requires the empirical distribution of planet detections to be corrected for imperfect survey completeness. The completeness correction is treated separately for each subset of planets from *Kepler* or *K2* in the following subsections. Each set of corrections accounts for detection biases arising from the imperfect detection sensitivity and for the geometric probability of a planetary transit to occur.

4.1. *Kepler Sensitivity*

The derivation of the *Kepler* planet detection sensitivity follows from the methodology outlined in Christiansen et al. (2016) and used by Fulton et al. (2017) to resolve the radius valley around FGK stars. Per-target *Kepler* completeness products for DR25 and the SOC 9.3 version of the *Kepler* pipeline (Jenkins et al. 2010) are available for all of the planet-host stars in our *Kepler* sample (Burke et al. 2015; Burke & Catanzarite 2017). Detection sensitivities (or efficiencies) were calculated via transiting planetary signal injections at the pixel level (Christiansen et al. 2015, 2017) which are subsequently processed by the *Kepler* pipeline transiting planet search (TPS) module from which the detection sensitivity as a function of the Multi-event statistic (MES) is computed as the fraction of injected signals that are successfully recovered by the pipeline.

The MES represents the level of significance of a transit signal at a specified transit duration ranging from 1.5-15 hours. Following Petigura et al. (2018) we adopt an alternative diagnostic for the transit signal significance in the form of the transit S/N

$$\text{S/N} = \frac{Z}{\text{CDPP}_D} \sqrt{n_{\text{transits}}(\mathbf{t}, P, T_0)} \quad (4)$$

where $Z = (r_p/R_s)^2$ is the transit depth assuming a non-

grazing transit (i.e. $b \lesssim 0.9$), CDPP_D is the Combined Differential Photometric Precision on the timescale of the transit duration D, and n_{transits} is the number of observed transits given the target's data span and duty cycle[5] of observations $\mathbf{t}$, the planet's orbital period P, and its time of mid-transit T_0.

To compute the *Kepler* detection sensitivity as a function of S/N, we first derive the mapping between the MES and the transit S/N using the data from Christiansen et al. (2015) who derived the detection sensitivity of the *Kepler* pipeline from one year of data. The parameters of the injected planets are provided along with their corresponding MES and CDPP at each value of D considered. For each injected planet we interpolate its MES and CDPP values to D and calculate the transit S/N using Eq. 4. The mapping between MES and S/N is shown in Fig. 4 for the full set of injected planets whose transit S/N values span 2.7-4843. Given the large number of injected planetary signals ($> 10^4$), we fit the number-weighted S/N to MES mapping using the `scipy.curve_fit` non-linear least squares algorithm with a powerlaw function of the form $\text{MES} = A \cdot \text{S/N}^\alpha$. We find a best-fit amplitude and powerlaw index of $A = 0.977$ and $\alpha = 0.967$ respectively with negligible uncertainties. This relation is used to map the transit S/N to MES which is then mapped to the detection sensitivity. The average *Kepler* detection sensitivity curve as a function of transit S/N, along with the 16th and 84th percentiles for the stars in our *Kepler* sample are shown in Fig. 5.

4.2. *K2 Sensitivity*

Unlike the primary *Kepler* mission, the *K2* data products do not feature detailed completeness and reliability products. To derive the detection sensitivity among the *K2* stars in our sample we employ the transit detection pipeline `ORION` (Cloutier 2019). The failure of the second reaction wheel on board the *Kepler* spacecraft in 2013 prevented the observatory from maintaining the fine pointing accuracy required to obtain ultra precise photometry. The re-purposed *K2* mission exploited the solar wind pressure by enabling the observatory to continue pointing along the ecliptic plane with realignments via thrusters firings **every ∼ 6 hours** (Howell et al. 2014). `ORION` lacks a module to correct for the temporally correlated pointing corrections so as input we feed the `EVEREST` light curves which use a pixel level decorrelation to remove systematics from the spacecraft's variable pointing (Luger et al. 2016, 2018). We favor the `EVEREST` *K2* light curves over light curves produced by similar pipelines (e.g. `K2SFF`; Vanderburg & Johnson 2014, `K2SC`; Aigrain et al. 2015, 2016) due to its performance in obtaining improved photometric precision at the level of ∼ 20 − 50% (Luger et al. 2016).

We quantify the *K2* detection sensitivity using `ORION` by first retrieving the `EVEREST` light curve from MAST for each star in our sample. We only consider light curves from individual campaigns. As `ORION` input we supply the time sampling $\mathbf{t}$ in BJD, the corrected flux, and flux uncertainties in e$^-$/second, from the `EVEREST` keywords `TIME`, `FCOR`, and `FRAW_ERR`. The duty cycle is derived by restricting ourselves to light curve measurements for

---

[5] Number of useful cadences for transit signal detection.

FIG. 3.— Empirical population of confirmed close-in planets around low mass stars. The distribution of 275 and 53 confirmed planets from *Kepler* and *K2* respectively as a function of orbital period, insolation, and planet radius. The two-dimensional maps are Monte-Carlo sampled from the measurement uncertainties on the planetary radii and insolations while the fractional uncertainties on the orbital periods are inflated to 20%.

TABLE 1
Kepler CONFIRMED PLANET PARAMETERS

KIC	Planet name	P [days]	F [$F_\oplus$]	F upper limit [$F_\oplus$]	F lower limit [$F_\oplus$]	r_p [$R_\oplus$]	r_p upper limit [$R_\oplus$]	r_p lower limit [$R_\oplus$]
1873513	Kepler-1624 b	3.29030	36.3	5.9	5.5	6.53	0.19	0.20
2556650	Kepler-1124 b	2.85235	47.4	5.0	4.6	1.97	0.08	0.10
2715135	Kepler-753 b	5.74771	41.3	5.1	4.8	1.89	0.30	0.12
3234598	Kepler-383 b	12.90468	20.6	3.2	2.5	1.54	0.30	0.17
3234598	Kepler-383 c	31.20122	6.4	0.9	0.7	1.49	0.34	0.22

TABLE 2
K2 CONFIRMED PLANET PARAMETERS

EPIC	Planet name	P [days]	F [$F_\oplus$]	F upper limit [$F_\oplus$]	F lower limit [$F_\oplus$]	r_p [$R_\oplus$]	r_p upper limit [$R_\oplus$]	r_p lower limit [$R_\oplus$]
201110617	K2-156 b	0.81315	1146.7	5038.8	734.4	1.35	0.12	0.10
201155177	K2-42 b	6.68796	93.9	353.9	58.8	2.45	0.27	0.25
201205469	K2-43 b	3.47114	83.9	316.0	52.2	4.09	0.28	0.25
201208431	K2-4 b	10.00440	34.2	167.1	23.5	2.52	0.34	0.31
201338508	K2-5 b	5.73597	47.3	209.2	29.5	1.95	0.17	0.18

FIG. 4.— Correlation between the *Kepler* multi-event statistic and transit S/N. The mapping between the MES and S/N based on the synthetic planetary signals injected into the *Kepler* pipeline (Christiansen et al. 2015). The number-weighted powerlaw fit (*solid line*) to the correlation differs slightly from a one-to-one relation (*dashed line*) with the.

FIG. 5.— Average detection sensitivity for *Kepler* and *K2*. The *solid curves* represent the average transiting planet detection sensitivity for the *Kepler* and *K2* stars in our sample as a function of the transit S/N (Eq. 4). The shaded regions mark the 16th and 84th percentiles of the measured detection sensitivities.

which the QUALITY flag is zero. Any known signals from planets, PCs, or FPs are removed from the light curve based on their reported transit parameters using the batman (Kreidberg 2015) implementation of the Mandel & Agol (2002) transit model. We then inject transiting planetary signals directly into the light curve by sampling planets from the linear transit S/N grid $\mathcal{U}(0, 50)$. The per-system multiplicity is drawn from the cumulative occurrence rate of small planets out to 200 days around mid-K to early M dwarfs from *Kepler* (2.5 ± 0.2; Dressing & Charbonneau 2015). Each planet's time of mid-transit T_0 is drawn from $\mathcal{U}(\min(\mathbf{t}), \max(\mathbf{t}))$. In a given light curve, with a fixed CDPP(D) and $\mathbf{t}$, for a star whose radius and mass are fixed to their maximum likelihood values, we draw each planet's logarithmic orbital period from $\mathcal{U}(\log_{10}(0.5 \text{ days}), \log_{10}(200 \text{ days}))$ which allows us to compute the number of transits that occur within $\mathbf{t}$. Note that some injected planets will exhibit $n_{\text{transits}} = 0$ due to the limited *K2* baselines of typically ~ 80 days. The drawn orbital period also uniquely determines the planet's radius corresponding to its drawn value of the S/N. To ensure dynamical stability in multi-planet systems, we compute the maximum likelihood planet mass from the probabilistic mass-radius relation forecaster

(Chen & Kipping 2017) and analytically assess the Lagrange stability of each neighboring planet pair assuming circular orbits (Barnes & Greenberg 2006). Each planet's scaled semimajor axis a/R_s and scaled radius r_p/R_s follow from their sampled radius r_p and the stellar parameters R_s and M_s. We sample impact parameters b from $\mathcal{U}(0, 0.9)$ to compute the orbital inclinations. Furthermore, we adopt fixed quadratic limb darkening coefficients by interpolating the *Kepler* bandpass coefficient grid along T_{eff}, $\log g$, and [Fe/H], assuming solar metallicity when [Fe/H] measurements are absent (Claret et al. 2012). These parameters are used to compute transit models in the absence of any transit timing variations. Transit signals are then injected into the cleaned *K2* light curves and fed to ORION to conduct a blind search for transiting signals.

The detection sensitivity as a function of S/N for each *K2* star is computed by considering a minimum of 10^2 injected planetary systems per star and computing the recovery fraction of injected small planets with $P \leq \mathbf{100}$ days. The average *K2* detection sensitivity curve, along with the 16th and 84th percentiles, are also included in Fig. 5. The quality of the pointing corrections within the EVEREST light curves can vary widely within our sample such that there is considerably more variance in the *K2* detection sensitivity relative to *Kepler*. Furthermore, the average detection sensitivity is significantly reduced compared to *Kepler*. The reduced sensitivity is due in-part to the imperfect corrections of the reduced pointing accuracy and to the limited time baseline of ~ 80 days in a typical *K2* light curve compared to *Kepler*. Furthermore, we have not attempted to optimize the performance of ORION on *K2* light curves beyond slight modifications to the algorithm's performance hyperparameters that were made to ensure the detection of 52/53? confirmed

K2 planets. The planet K2-21c (EPIC 206011691.02, $P = 15.5$ days) remains undetected by `ORION` because of the algorithm's requirement to discard putative signals that are commensurate with other high S/N signals in the light curve. The presence of K2-21b at $P = 9.32$ days is within 1% of a 5:3 period ratio with K2-21c and thus inhibits the identification of the 15.5 day signal as being independent and planetary.

4.3. *Two-dimensional sensitivity maps*

The sensitivity curves depicted in Fig. 5 enable us to extend the visualization of the detection sensitivity to two dimensions. Explicitly, we consider the detection sensitivity s_{nij} for each star (indexed by n) and as a function of P and r_p which are indexed by i and j respectively. Consideration of the sensitivity in the $P-r_p$ plane will be needed to evaluate the occurrence rates in that parameter space which is important for understanding the structure of the radius valley around low mass stars due to the dependence of the efficiency of atmospheric loss on both planet size and separation, regardless of the physical mechanism involved.

We consider orbital periods $P \in [0.5, 100]?$ days and planet radii $r_p \in [0.5, 4]$ R$_\oplus$. At each grid cell nij we compute the average S/N within the cell and map that value to the detection sensitivity using the data in Fig. 5. The detection sensitivity maps for *Kepler* and *K2*, averaged over the index n, are shown in Fig. 6.

4.4. *Survey Completeness*

Only transiting planets are detectable in transit surveys. To correct for the non-detection of otherwise detectable but non-transiting planets we compute the geometric transit probability for each star n and at each grid cell ij in the $P - r_p$ space to be

$$p_{t,nij} = \frac{R_{s,n} + r_{p,j}}{a_{ni}}. \tag{5}$$

Note that we are only interested in the relative planet occurrence rate and therefore do not consider constant scalar modifications to $p_{t,nij}$ from effects such as grazing transits or non-zero eccentricities (Barnes 2007).

The product of each star's detection sensitivity with its geometric transit probability yields completeness maps as a function of P and r_p. The average completeness maps for our *Kepler* and *K2* stars are shown in Fig. 7.

5. THE OCCURRENCE RATE OF SMALL CLOSE-IN PLANETS AROUND LOW MASS DWARF STARS

5.1. *Occurrence rates versus orbital period and planet radius*

The detection and validation of planets from the *Kepler* and *K2* missions enable to measurement of the occurrence rate of planets given the completeness corrections derived in Sect. 4. For the index i representing a planet's orbital period and j representing the planetary radius, the probability of detecting an integer number of planets within that grid cell (k_{ij}) around N_s stars is given by the binomial likelihood function

$$\mathcal{L}_{nij}(k_{ij}|N_s, P_{nij}) = \binom{N_s}{k_{ij}} \prod_{n=1}^{N_s} P_{nij}^{k_{ij}}(1-P_{nij})^{N_s-k_{ij}} \tag{6}$$

where

$$P_{nij} = s_{nij} \cdot p_{t,nij} \cdot f_{ij}, \tag{7}$$

is the probability of detecting a planet in the ij grid cell around the nth star. This quantity is dependent on the detection sensitivity s_{nij}, the transit probability $p_{t,nij}$, and the intrinsic occurrence rate of planets in the grid cell ij: f_{ij}. The number of planet detections k_{ij} is depicted in Fig. 3 for i representing the orbital period and insolation. Together with our calculations of s_{nij} and $p_{t,nij}$ for the $N_s = 17393$ low mass stars in our sample (Figs. 6 and 7), and noting from Bayes theorem that the posterior probability of f_{ij} is

$$p(f_{ij}|N_s, s_{nij}, p_{t,nij}, k_{ij}) \propto \mathcal{L}_{nij}(k_{ij}|N_s, s_{nij}, p_{t,nij}, f_{ij}), \tag{8}$$

modulo the coefficient of proportionality which we set to unity.

Firstly, recall that there are ~ 5 times more confirmed planets from *Kepler* than from *K2* in our sample (see Fig. 3) despite our sample having ~ 3.5 times more *K2* stars (see Fig. 2). These factors compound to produce a lower planet occurrence rate measured with *K2* than with *Kepler* as the reduced *K2* detection completeness (see Fig. 7) is insufficient to account for the lower measured planet occurrence rates. The discrepancy instead arises from the disparate resources that have been dedicated to the confirmation of planets from *Kepler* and *K2*. The result being that the number of confirmed planets existing within the set of *K2* PCs is underestimated by the number of PCs that have been reported as validated so far. We address this discrepancy by scaling the cumulative occurrence rate measured by *K2* in our sample to that of *Kepler*. In this way, we are assuming that the planet populations studied by each mission are inherently identical despite existing within distinct stellar populations within the galaxy.

The maximum a-posteriori (MAP) map of f_{ij} is depicted in Fig. 8. The persistence of the radius valley from Sun-like to the low mass stars in our sample is clearly evident. Distinct peaks are separated along the planetary radius axis and span $\sim 0.9 - 1.4$ R$_\oplus$ and $\sim 1.9 - 2.3$ R$_\oplus$ respectively. Note however that the lower limit on the former peak nearly approaches the region in which the *Kepler* sensitivity falls below 10% and the f values become unreliable. The occurrence rates also highlight the relative dearth of planets larger than ~ 3 R$_\oplus$ including the Neptunian desert at short orbital periods (Lundkvist et al. 2016; Mazeh et al. 2016). The large scale structure of the measured occurrence rates are also broadly consistent with previous investigations of the planet population around low mass *Kepler* stars (Dressing & Charbonneau 2013, 2015; Gaidos et al. 2016) such as the prominence of planets $\lesssim 2$ R$_\oplus$ with $P \sim 10 - 60$ days and a cumulative occurrence rate of 2.87? planets per star.

The location and slope of the radius valley (i.e. $d \log r_p / d \log P$) are broadly consistent with the valley structure measured from the empirical planet population of FGK stars characterized via asteroseismology (Van Eylen et al. 2018). Wu (2019) also provided a visual approximation to the location of the radius valley around stars with $M_s \in [0.5, 0.76]$ M$_\odot$ in their *Gaia-Kepler* sam-

FIG. 6.— Average detection sensitivity versus orbital period and planetary radius. The detection sensitivity maps averaged over *Kepler* stars (*left panel*) and over *K2* stars (*right panel*) from our sample of low mass dwarf stars.

FIG. 7.— Average completeness versus orbital period and planetary radius. Maps of the product of the detection sensitivity and geometric transit probability averaged over *Kepler* stars (*left panel*) and over *K2* stars (*right panel*) from our sample of low mass dwarf stars.

FIG. 8.— Planet occurrence rate versus orbital period and planetary radius. The maximum a-posteriori occurrence rate map calculated from the population of confirmed planets from *Kepler* (*circles*) and *K2* (*diamonds*) around low mass dwarf stars. Overplotted are the empirical locations of the radius valley around FGK stars characterized via asteroseismology (*dashed line*, Van Eylen et al. 2018) and the approximate radius valley around early-M to mid-K dwarfs (*dotted line*, Wu 2019).

ple. However we find the location of the terrestrial-sized planet peak to exist at longer $P \sim 30$ days compared to ~ 5 days (c.f. Fig. 2, Wu 2019). The discrepancy likely stems from differences in the methods of correcting for survey incompleteness. Recall that in this study the detection sensitivity is computed for each star using it's unique completeness products from the *Kepler* pipeline whereas Wu (2019) adopt piecewise completeness levels of 10, 50, or 90% complete as a function of P and r_p from Zhu et al. (2018).

Lastly, we note that the radius valley as a function of P does not appear to be completely void of planets. This may present evidence of the efficiency of the gap clearing mechanism around low mass stars and is discussed further in Sect. 7.3.

5.2. Occurrence rates versus planet radius

Next we marginalize over P and compute the one-dimensional occurrence rate of small, close-in planets as a function of r_p. The resulting occurrence rates are shown in Fig. 9 in which the bimodal distribution of planet sizes is again clearly discernible in the MAP occurrence rates. The uncertainties on each f_j bin are computed from the 16th and 84th percentiles of the f_j posterior. We ignore the occurrence rates in bins with $r_p \lesssim 1$ R$_\oplus$ where our detection sensitivity is poor.

From the bimodal distribution we highlight the approximate radii likely corresponding to planets with terrestrial bulk compositions ($r_p \lesssim 1.55$ R$_\oplus$) versus planets with significant size fractions in gaseous envelopes ($r_p \gtrsim 1.55$ R$_\oplus$) around low mass stars. Also depicted in Fig. 9 is f_j with a binning scale twice that of the primary f_j depiction (i.e. 0.06 R$_\oplus$ compared to 0.13 R$_\oplus$). With this adopted fine binning the fractional uncertainties on f_j in each bin are sufficiently large to eliminate the significance of the distinct bimodal peaks. Despite this, the bimodality in the MAP occurrence rates continues to persist with the location of the valley features only being marginally affected. We interpret this as further evidence for the existence of the radius valley in the close-in planet population around low mass stars.

5.3. Inclusion of supplemental K2 planet candidates

In an attempt to improve the counting statistics in the occurrence rate calculations, we consider an enlarged planet population. This population is the union of our confirmed planet sample with a set of additional planet candidates (PCs) from the *K2* mission. Specifically, we consider the set of PCs reported by Kruse et al. (2019) from *K2* campaigns 0-8 that includes 126 PCs not already included in our sample of confirmed planets and orbiting stars contained within our stellar sample.

By definition, we cannot identify which PCs are true planets of interest for this study and which PCs are instead produced by an astrophysical false positive. The inclusion of *K2* PCs therefore requires that we account for sample contamination by false positives probabilistically. We do so by considering a number of studies from the literature that perform a transiting planet search in *K2*, from any subset of its campaigns, and present attempts at validating their uncovered PCs statistically based on follow-up observations (Montet et al. 2015; Crossfield et al. 2016; Dressing et al. 2017; Hirano et al. 2018; Livingston et al. 2018; Mayo et al. 2018). Each of these studies utilized some combination of ground-based photometry to validate planet ephemerides, reconnaissance spectroscopy to identify spectroscopic binaries, and speckle or AO-assisted imaging to search for nearby stellar companions to their PC host stars. Each of the aforementioned studies used their respective set of follow-up observations together with the statistical validation tool `vespa` (Morton 2012, 2015) to statistically classify their PCs as either a validated planet (VP)[6], a false positive (FP), or some other inconclusive disposition (e.g. remains a PC). The FP rate around cool stars ($T_{\rm eff} < 4700$ K) from each study is estimated by calculating the ratio of the number of reported FPs to the total number of FPs and VPs. Notably, Crossfield et al. (2016) showed that the FP rate in their *K2* sample is dependent on the measured planet radius as giant PCs have a larger likelihood of being a FP. Hence, we focus on PCs with $r_p < 4$ R$_\oplus$ when deriving FP rates.

The resulting FP rates are reported in Table 3. Half of the studies do not find any probable FP signals among the small PCs orbiting cool stars in their samples. In such cases only upper limits on the FP rate can be derived which all agree that the FP rate is $\lesssim 20\%$ at 95%. The remaining studies each detect at least one FP such that a non-zero maximum likelihood FP rate is measured. Their average FP rate is 5.7% which is also in agreement with the derived upper limits from the aforementioned studies. We proceed by constructing 10^3 realizations of the planet population that includes confirmed planets from both *Kepler* and *K2* plus a subset of the 126 *K2* PCs from Kruse et al. (2019). The subset of included PCs are randomly sampled from the full PC set according to the adopted FP rate such that each realization contains $0.943 \cdot 126 \approx 119$ PCs.

The effect of including PCs in the planet sample on the derived occurrence rates are compared to the results from only considering confirmed planets in Fig. 10. Again we scale the *K2* occurrence rates to those from *Kepler* such that the cumulative occurrence of close-in planets with $r_p \leq 4$ R$_\oplus$ is identical between the two planet popula-

---

[6] We treat validated and confirmed planets as equivalent dispositions.

FIG. 9.— Occurrence rate of planets as a function of size. *Upper panel*: histogram depicting the relative occurrence rate of close-in planets with orbital periods < 100 days derived from the population of confirmed *Kepler* and *K2* planets around low mass stars. The bimodal distribution of planet radii peaking at 1.12 and 2.07 $R_\oplus$ highlights the presence of the radius valley around low mass stars centered at 1.54 $R_\oplus$. Uncertainties in the planet occurrences follow from binomial statistics and are limited by the relatively small number of confirmed planets around low mass stars from *Kepler* and *K2*. The measured occurrence rates below ~ 1 $R_\oplus$ (shown in *grey*) should be ignored due to the poor detection sensitivity. *Lower panel*: identical occurrence rates as in the upper panel accompanied by the same occurrence rates with finer radius bins. The corresponding occurrence rate uncertainties are too large to robustly infer the presence of features but the bimodal structure continues to be exhibited in the maximum likelihood occurrence rates. The shaded regions highlight our approximate definitions of terrestrial planets ($r_p \in [0.97, 1.57]$ $R_\oplus$), down to reasonable sensitivity limits, and gaseous planets ($r_p > 1.57$ $R_\oplus$) around low mass stars. Note the outer limit of 2.5 $R_\oplus$ is arbitrary.

TABLE 3
K2 FALSE POSITIVE RATES FOR
SMALL PLANETS AROUND COOL STARS

Reference	$N_{\rm FP}$	$N_{\rm VP}$	FP rate [%]
Montet et al. (2015)[a]	0	8	< 30.7
Crossfield et al. (2016)	2	39	$4.9^{+6.0}_{-1.4}$
Dressing et al. (2017)	2	34	$5.6^{+6.4}_{-2.0}$
Hirano et al. (2018)[a]	0	16	< 19.5
Livingston et al. (2018)[a]	0	14	< 21.0
Mayo et al. (2018)[b]	1	14	$6.7^{+12.4}_{-2.0}$

NOTE. — Within each study we only consider PCs with $r_p < 4$ $R_\oplus$ and orbiting cool stars with $T_{\rm eff} < 4700$ K. FP: false positive. VP: validated planet.

[a] These studies do not detect any FPs such that the reported FP rate upper limit is represented by its 95% confidence interval.

[b] Mayo et al. (2018) did not explicitly classify their non-validated planets as FPs so we define FPs within their sample as any PC whose false positive probability exceeds 10%.

tions. The radius valley continues to be resolved in the MAP occurrence rates. Furthermore, the addition of PCs reduces the median f_j uncertainty among planets with $r_p > 1$ $R_\oplus$ from 0.0216 to 0.0186 planets per star (i.e. $\sim 15\%$ improvement). However, the partial filling of the gap is increased as the contrast between the maximum f_j of the terrestrial planet peak ($r_p \sim 1.3$ $R_\oplus$) and the minimum f_j of the valley ($r_p \sim 1.6$ $R_\oplus$) decreases from 0.070 $R_\oplus$ (3.2σ) to 0.054 (2.9σ).

6. EVOLUTION OF THE RADIUS VALLEY AROUND LOW MASS STARS

6.1. *Slope of the radius valley*

Fig. 11 shows the two-dimensional occurrence rate of close-in small planets in the $F - r_p$ space. This depiction enables the comparison of the close-in planet population around low mass stars to the population around Sun-like stars (Fulton et al. 2017). It also enables the calculation of the slope of the radius valley with F which can then be compared to model predictions of the planet size marking the transition from terrestrial to gaseous planets versus insolation. We measure the slope of the valley by sampling planets from the inverse occurrence rates over the domains $F \in [1, 30]$ $F_\oplus$ and $r_p \in [1, 2.5]$ $R_\oplus$ such that the valley, where planets are less common in nature, dominate this synthetic population. The relative number of sampled planets is then fit with a linear function in the $\log F - r_p$ space depicted in Fig. 11. From

10^3 realizations of the resampled planet population we measure the average slope and its standard deviation to be $\mathrm{d}r_p/\mathrm{d}\log F = -0.093 \pm 0.010$. Similarly, in the $P - r_p$ space we measure $\mathrm{d}r_p/\mathrm{d}\log P = 0.191 \pm 0.011$.

The negative slope $\mathrm{d}r_p/\mathrm{d}\log F$ indicates that the location of the radius valley drops to smaller planet radii with increasing insolation (i.e. decreasing orbital period). This behavior is broadly consistent with models of the radius valley formation from the formation small terrestrial of bodies in a gas-poor environment (Lee et al. 2014; Lee & Chiang 2016; Lopez & Rice 2018). The theoretical scaling of the transition radius with insolation in the gas-poor formation scenario is $r_{p,valley} \propto F^{-0.08}$ (Lopez & Rice 2018) which is consistent with our measured scaling of -0.093 ± 0.010. This result is inconsistent with the models of photoevaporation and core-powered mass loss which each predict an increasing central valley radius with increasing insolation ($r_{p,valley} \propto F^{0.11}$; Lopez & Rice 2018, $r_{p,valley} \propto F^{0.10}$; Gupta & Schlichting 2019b).

The negative slope in the radius valley around low mass stars differs from the trend seen around Sun-like stars (Fulton et al. 2017). Fig. 11 compares the occurrence rates of small close-in planets around each stellar population. Multiple studies have concluded that the location of the radius valley around Sun-like stars drops to smaller planet sizes with decreasing insolation (e.g. Van Eylen et al. 2018; Martinez et al. 2019). Conversely, Fig. 11 indicates that the opposite may be true around low mass stars. This observational evidence may elucidate changes in the dominant physical mechanisms that sculpt the valley around different host spectral types.

6.2. *Planet populations versus stellar mass*

In addition to calculating the occurrence rates f_{ij} among our full stellar sample, we also consider the evolution of the planet population in unique host stellar mass bins. Fig. 12 shows the MAP f_{ij} maps in $P - r_p$ space and the marginalized f_j distributions in four stellar mass bins: our full stellar sample ($M_s \in [0.08, 0.93]$ $M_\odot$), the massive half of the sample ($M_s > 0.65$ $M_\odot$), the low mass half of the sample ($M_s < 0.65$ $M_\odot$), and a subset of the latter focusing on increasingly lower mass stars ($M_s < 0.42$ $M_\odot$). The statistically significant resolution of the radius valley in the f_j occurrence rates is only accomplished with the full stellar sample. The reduction of the sample size in the three remaining mass bins inflates the f_j uncertainties such that the valley is seen at $< 1\sigma$ and hence not detected. However, the characteristic bimodality is exhibited in the MAP f_{ij} of the full and massive half stellar samples. Furthermore, their f_{ij} structures are similar as the majority of our full planet sample orbit stars more massive than the median stellar mass of 0.65 $M_\odot$ ($\sim 62\%$).

In considering stars less massive than 0.65 $M_\odot$, the

FIG. 10.— Comparison of occurrence rates with and without planet candidates included. *Left panel*: same as Fig. 9. *Right panel*: histogram depicting the relative occurrence rate of close-in planets with orbital periods < 100 days derived from the population of confirmed planets from *Kepler* and *K2* and supplemented by 119 PCs around low mass stars from Kruse et al. (2019). The radius valley continues to be resolved with the inclusion of PCs which improve the median uncertainty on the occurrence rate bins although the gap becomes less prominent with numerous PCs partially filling the valley.
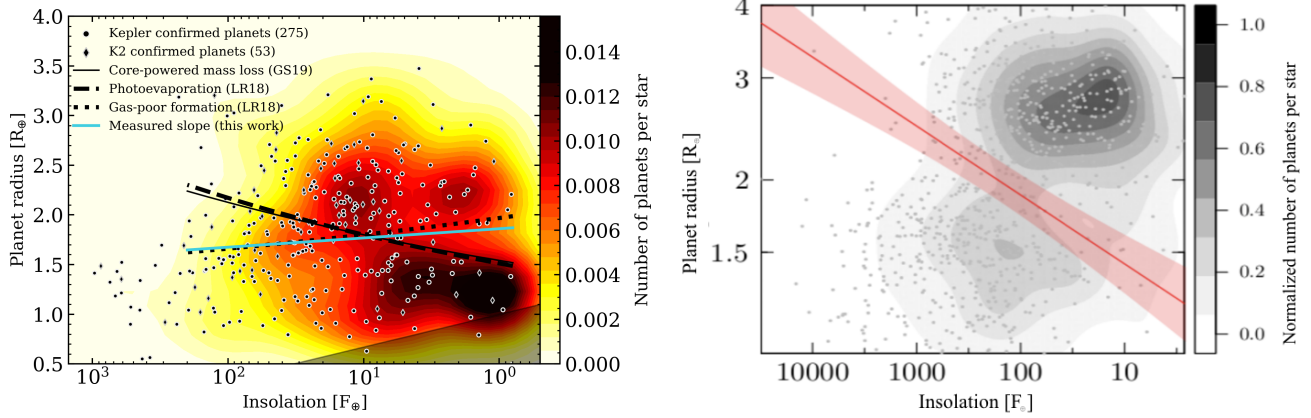

FIG. 11.— Planet occurrence rates versus insolation and planetary radius around low mass and Sun-like stars. *Right panel*: the maximum a-posteriori occurrence rate map calculated from the population of confirmed planets from *Kepler* (*circles*) and *K2* (*diamonds*) around low mass dwarf stars. Overplotted in black are model predictions of the transition from terrestrial to gaseous planets in the following scenarios: core-powered mass loss (Gupta & Schlichting 2019b), photoevaporation (Lopez & Rice 2018), and gas-poor formation Lopez & Rice (2018). We measure the slope of the radius valley to be $\mathrm{d}r_p/\mathrm{d}\log F = -0.093 \pm 0.010$ which is broadly consistent with predictions from gas-poor formation of terrestrial planets.

FIG. 12.— 2D and 1D planet occurrence rates in various stellar mass bins. *Top panels*: planet occurrence rate maps as a function of orbital period and planet radius. *Bottom panels*: distributions of the relative planet occurrence rate as a function of planet size. Note the differing occurrence rate scales. Each column corresponds to a unique cut in stellar masses which represent the full stellar sample ($M_s \in [0.08, 0.93]$ $\mathrm{M}_\odot$), the early half of the stellar sample ($M_s \in [0.65, 0.93]$ $\mathrm{M}_\odot$), the late half of the stellar sample ($M_s \in [0.08, 0.65]$ $\mathrm{M}_\odot$), and the low mass bin ($M_s \in [0.08, 0.42]$ $\mathrm{M}_\odot$) depicting a subset of the late half of the stellar sample. The relative occurrence of terrestrial to gaseous planets appears to increase around lower mass stars.

gaseous planet peak begins to diminish relative to the terrestrial-sized planets. As evidenced in the MAP f_j distribution around stars with $M_s \in [0.08, 0.65]$ $\mathrm{M}_\odot$, the radius valley might persist around 1.6 $\mathrm{R}_\oplus$ but the gaseous planet peak does not appear distinct from the terrestrial planet peak in the MAP f_{ij} map. That is that the relative frequency of terrestrial to gaseous planets appears to increase significantly around M dwarfs compared to the more massive K dwarfs. This feature is further accentuated around the lowest mass stars in our sample (< 0.42 $\mathrm{M}_\odot$) for which terrestrial-sized planets clearly dominate the distribution of close-in planets. The relative frequency of terrestrial to gaseous planets in each stellar bin are reported in Table 4 for fixed definitions of $r_p \in [1, 1.6]$ $\mathrm{R}_\oplus$ and $r_p \in [1.6, 2.5]$ $\mathrm{R}_\oplus$ respectively. The inner limit of 1 $\mathrm{R}_\oplus$ restricts this analysis to where the detection sensitivity is still informative. The outer limit of 2.5 $\mathrm{R}_\oplus$ is chosen such that the full width at half maximum of the gaseous planet peak in the f_j distribution from the full stellar sample (Fig. 9) is approximately identical for each peak.

The values in Table 4 indicate the significant increase in the relative occurrence of terrestrial planets with decreasing stellar mass that is also illustrated in Fig. 12. This is evidenced by our measurements showing that gaseous planets are nearly twice as common as terrestrial planets around mid to late K dwarfs ($M_s \in [0.65, 0.93]$ $\mathrm{M}_\odot$) while the relative frequency approaches unity around M dwarfs ($M_s \in [0.08, 0.65]$ $\mathrm{M}_\odot$). Focusing on the lowest stellar mass bin considered, terrestrial planets become much more prominent as they outnum-

TABLE 4
RELATIVE OCCURRENCE RATES OF CLOSE-IN TERRESTRIAL
AND GASEOUS PLANETS AROUND LOW MASS STARS

Stellar mass range [$\mathrm{M}_\odot$]	f_{terr} $r_p \in [1, 1.6]$	f_{gas} $r_p \in [1.6, 2.5]$	$f_{\mathrm{terr}}/f_{\mathrm{gas}}$
[0.08, 0.90]	0.68 ± 0.07	1.02 ± 0.08	0.66 ± 0.09
[0.63, 0.90]	0.69 ± 0.11	1.28 ± 0.16	0.54 ± 0.11
[0.08, 0.63]	1.10 ± 0.16	1.02 ± 0.16	1.08 ± 0.23
[0.08, 0.42]	1.64 ± 0.43	0.19 ± 0.09	8.46 ± 4.62

ber gaseous planets by a factor of 8.46 ± 4.62. This result is broadly consistent the calculations of Hardegree-Ullman et al. (2019) who find that terrestrial-sized planets with $r_p \in [0.5, 1.5]$ $\mathrm{R}_\oplus$ are about $4 - 5$ times as common as gaseous planets () around M3-5.5 dwarfs ($M_s \in [0.12, 0.38]$ $\mathrm{M}_\odot$). Thus we have supporting evidence

6.3. *Dependence of radius valley features on stellar mass*

Here we measure the locations and uncertainties of features in the radius valley in each of the stellar mass bins considered in Sect. 6.2. In each of the four f_{ij} occurrence rate maps shown in Fig. 12, we measure the frequency-weighted central radius of the terrestrial planet peak, the gaseous planet peak, and the radius valley. We quantify the uncertainties in the feature locations by marginalizing over the following hyperparameters that can directly affect the inferred radius of each feature: the f_{ij} smoothing parameter, the minimum detection sensitivity, the P bin width, the r_p bin width, along with the imposed

upper and lower P and r_p limits on each peak. These upper and lower r_p limits are defined based on the visual inspection of the f_{ij} maps in Fig. 12 and are used to demarcate the assumed boundaries of each peak, and by extension the valley separating the peaks. For example, if the boundaries on the terrestrial peak are set to 1-50 days and 0.8-1.4 $R_\oplus$ then only the planet occurrence rates over that subset of the $P - r_p$ parameter space are considered when calculated the f_j-weighted peak radius. The boundaries are listed in Table 5. In practice we derive 10^3 realizations of each f_{ij} map with each realization having a unique set of hyperparameters. The resulting f_{ij} maps are marginalized over P and the f_j-weighted radius of each peak is computed over the domain bounded by the relevant hyperparameters (see Table 5). The same is done for the radius valley using the inverse occurrence rates.

The resulting locations of each radius peak and the valley are depicted in Fig. 13 as a function of stellar mass and given explicitly in Table 6. The depicted M_s values are given by the median and with uncertainties given by the 16$^{\text{th}}$ and 84$^{\text{th}}$ percentiles. In computing the feature locations we assume that the radius valley is present in all stellar mass bins despite the waning evidence for its existence around stars with $M_s \lesssim 0.4$ $M_\odot$ (see Fig. 12). Our measured feature radii are compared to those measured in Fulton & Petigura (2018) around Sun-like stars with $M_s < 0.97$, $\in [0.97, 1.11]$, and > 1.11 $M_\odot$. Most notably, the feature locations obtained from our full stellar sample continue to the trend of monotonically decreasing to smaller r_p with decreasing M_s. The slopes of this decrease for the terrestrial and gaseous planet peaks are $dr_{p,\text{terr}}/dM_s = 0.40$ and $dr_{p,\text{gas}}/dM_s = 0.97$ respectively indicating that the most common size of gaseous planet decreases more steeply with M_s than the typical size of terrestrial planets. We interpret this as being indicative of the effective disappearance of gaseous planets around increasingly lower mass stars (see Table 4). Furthermore, the reduced slope of the terrestrial peak may be indicative of a characteristic planetary core size of ≈ 1 $R_\oplus$.

Models of the formation of the radius valley based upon photoevaporation (Wu 2019), gas-poor formation (Lopez & Rice 2018), and core-powered mass loss (Gupta & Schlichting 2019b) all make explicit predictions for the evolution of the radius valley location with stellar mass. Predictions from the core-powered mass loss scenario are dependent on the stellar mass-luminosity relation (MLR) $L_s \propto M_s^\alpha$. In Fig. 13, we consider cases with a constant MLR with $\alpha = 5$ (Gupta & Schlichting 2019b) and with the empirically-derived piecewise MLR from Eker et al. (2018). All models predict a decreasing radius valley with decreasing stellar mass but differ in their slopes. At the median stellar mass of our full stellar sample (0.65 $M_\odot$), the measured location of the radius valley is 1.54 ± 0.16 $R_\oplus$. This value favors a steep dr_p/dM_s slope although we are unable to distinguish between competing physical models given the uncertainty in the location. Fortunately, the model predictions continue to diverge with decreasing stellar mass. As such, measurements of the feature locations in decreasing M_s bins can be used to rule out the operation of certain physical mechanisms in the low stellar mass regime. Athough the trend of decreasing median feature radii with decreasing stellar mass is upheld, the poor counting statistics in

the reduced M_s bins prevent any signficant inference regarding the relative strength of the competing physical mechanisms.

7. DISCUSSION & CONCLUSIONS

7.1. *Improving constraints on the occurrence rate of small close-in planets orbiting mid-M dwarfs*

The issue of having insufficient information to distinguish between photoevaporation, core-powered mass loss, and gas-poor formation around low mass stars can be addressed with two steps. Firstly, by expanding the low mass stellar sample in transiting searches for small close-in planets and secondly, by quantifying the detection sensitivity in those searches. NASA's Transiting Exoplanet Survey Satellite (*TESS*; Ricker et al. 2015) will provide hundreds of new transiting planet discoveries in the vicinity of the radius valley (Barclay et al. 2018). *TESS* is particularly well-suited to the discovery of close-in planets around low mass stars down to M5V ($M_s \sim 0.16$ $M_\odot$) due to its red bandpass (600-1000 nm) and its high cadence (2 minute) observations of 200,000-400,000 stars over $\sim 94\%$ of the sky following its recently approved extended mission.

The *TESS* primary mission, lasting one year, has been ongoing since July 2018. Based on the mission's performance at the time of writing, we can calculate the number of stars required to be observed by *TESS* to enable robust conclusions regarding the nature of the radius valley down to low mass stars. These calculations proceed by noting that based on binomial statistics, the measurement uncertainty on the feature locations scales as $\sqrt{N_s P(1-P)}$ where N_s is the number of observed stars and P is the probability of detecting a small close-in planet given the detection sensitvity, its transit proability, and its inherent rate of occurrence (see Eq. 7). Through sectors 1-14, *TESS* has observed $N_{s,\text{TESS}} = 23051$ stars less massive than 0.4 $M_\odot$ from its Candidate Target List (CTL; Stassun et al. 2019) with 2 minute cadence. Among these stars, the Science Processing Operations Center (SPOC; Jenkins et al. 2016; Twicken et al. 2018; Li et al. 2018) has reported three objects of interest spanning the radius valley between $1.4 - 1.6$ $R_\oplus$. Assuming a 0% false positive rate among these planet candidates and the same MAP occurrence rate as measured with *Kepler* ($f_{\text{valley}} \approx 0.19$ planets per star), we find the probability of *TESS* to detect a transiting planet spanning the radius valley around a star with $M_s < 0.4$ $M_\odot$ to be $P_{\text{valley,TESS}} = 1.30 \times 10^{-4}$. We can compare these to the *Kepler* values of $N_{s,\text{Kep}} = 33$ and $P_{\text{valley,Kep}} = 8.56 \times 10^{-3}$ to scale the uncertainty on f_{valley}, and hence on the valley radius, as an increasing number of low mass stars are observed with *TESS*.

The resulting improvement in the measurement precision of the radius valley is shown in Fig. 14. ??

7.2. *Implications for RV planet searches around low mass stars*

Many existing and up-coming RV spectrographs will be partially focused on characterizing the masses of planets spanning the radius valley in order to improve our physical understanding of the nature of those planets. The subset of those spectrographs operating in the near-IR, in particular, will focus heavily on M dwarf planetary sys-

TABLE 5
Assumed boundary ranges on the locations of radius valley features

Stellar mass range [M$_\odot$]	$\log P$ lower boundary [days]	$\log P$ upper boundary [days]	Terrestrial peak lower r_p boundary [R$_\oplus$]	Terrestrial peak upper r_p boundary [R$_\oplus$]	Gaseous peak lower r_p boundary [R$_\oplus$]	Gaseous peak upper r_p boundary [R$_\oplus$]
[0.08, 0.90]	$\mathcal{U}(\log 0.5, \log 2)$	$\mathcal{U}(\log 50, \log 100)$	$\mathcal{U}(0.8, 1)$	$\mathcal{U}(1.2, 1.5)$	$\mathcal{U}(1.6, 1.9)$	$\mathcal{U}(2.3, 2.5)$
[0.63, 0.90]	$\mathcal{U}(\log 0.5, \log 2)$	$\mathcal{U}(\log 50, \log 100)$	$\mathcal{U}(0.8, 1)$	$\mathcal{U}(1.3, 1.5)$	$\mathcal{U}(1.8, 2)$	$\mathcal{U}(2.4, 2.7)$
[0.08, 0.63]	$\mathcal{U}(\log 0.5, \log 2)$	$\mathcal{U}(\log 50, \log 100)$	$\mathcal{U}(0.6, 0.9)$	$\mathcal{U}(1.2, 1.4)$	$\mathcal{U}(1.8, 2)$	$\mathcal{U}(2.1, 2.3)$
[0.08, 0.42]	$\mathcal{U}(\log 0.5, \log 2)$	$\mathcal{U}(\log 50, \log 100)$	$\mathcal{U}(0.5, 0.7)$	$\mathcal{U}(1.3, 1.4)$	$\mathcal{U}(1.7, 1.8)$	$\mathcal{U}(1.8, 2)$

NOTE. — The r_p boundaries on the radius valley are given implicitly by the upper r_p limit on the terrestrial peak and the lower r_p limit on the gaseous peak.

FIG. 13.— Evolution of the radius valley features with stellar mass. *Solid markers*: the occurrence rate-weighted locations of the terrestrial planet peak (*red markers*), the radius valley (*black markers*) and the gaseous planet peak (*blue markers*) as a function of host stellar mass. Measurements around Sun-like stars with $M_s > 0.8$ M$_\odot$ are retrieved from Fulton & Petigura (2018) (*open circles*). Feature radii from our full sample with $M_s = 0.651^{+0.058}_{-0.096}$ M$_\odot$ are depicted as *filled circles*. *Filled squares* depict the feature radii from partitioning our sample into three M_s bins: $M_s \in [0.65, 0.93]$ M$_\odot$, $M_s \in [0.08, 0.65]$ M$_\odot$, and $M_s \in [0.08, 0.42]$ M$_\odot$. Uncertainties on the peak and valley locations are derived by sampling the measured occurrence rates and their uncertainties along with samples of the hyperparameters controlling map smoothing, minimum detection sensitivity, planet parameter binning, and the assumed feature ranges in P and r_p. The green curves represent theoretical predictions for the evolution of the radius valley with stellar mass based on physical models gas-poor terrestrial planet formation (*dotted*; Lopez & Rice 2018), core-powered atmospheric mass loss with an empirical mass-luminosity relation (*solid*; Gupta & Schlichting 2019b), a constant mass-luminosity relation (*dash-dotted*; Gupta & Schlichting 2019b), and photoevaporation (*dashed*; Wu 2019). The models only predict scaling relations with M_s and as such are anchored to the measured valley location at $M_s \sim$ M$_\odot$.

FIG. 14.— Expected improvement in the measurement precision of the radius peak and valley locations with additional confirmed planets around stars with $M_s \sim 0.3$ M$_\odot$. Assuming a fixed detection probability (**dont do this**), the shaded regions depict the degree of improvement in the upper and lower limits on location of the super-Earth peak (*blue*), the radius valley (*green*), and the sub-Neptune peak (*red*) as additional planets are detected by missions like TESS. For stars with $M_s \sim 0.3$ M$_\odot$, model predictions of the valley location from photoevaporation and core-powered mass loss differ by ~ 0.4 R$_\oplus$ (*dashed horinzontal line*). Based on the performance of TESS to-date, the expected time to confirm such planets is parameterized as a linear function of time and is depicted on the secondary x-axis.

TABLE 6
Radius valley features versus stellar mass

Stellar mass [M$_\odot$]	Terrestrial peak [R$_\oplus$]	Radius valley [R$_\oplus$]	Gaseous peak [R$_\oplus$]
$0.651^{+0.058}_{-0.096}$	$1.118^{+0.151}_{-0.148}$	$1.543^{+0.160}_{-0.160}$	$2.068^{+0.211}_{-0.205}$
$0.684^{+0.040}_{-0.035}$	$1.154^{+0.205}_{-0.239}$	$1.647^{+0.207}_{-0.215}$	$2.197^{+0.301}_{-0.256}$
$0.500^{+0.097}_{-0.146}$	$1.036^{+0.297}_{-0.308}$	$1.599^{+0.340}_{-0.352}$	$2.048^{+0.191}_{-0.199}$
$0.343^{+0.057}_{-0.092}$	$1.017^{+0.700}_{-0.807}$	$1.548^{+0.515}_{-0.496}$	$1.815^{+0.260}_{-0.192}$

NOTE. — As depicted in Fig. 13.

tems (e.g. CARMENES; Quirrenbach et al. 2014, HPF; Mahadevan et al. 2012, IRD; Kotani et al. 2014, NIRPS; Bouchy et al. 2017, SPIRou; Donati et al. 2018). In defining target samples that are equally complete on either side of the radius valley, it is critically important that the transition location between terrestrial and gaseous planets is known. In our full stellar sample which includes mid to late K dwarfs, the measured radius valley location is 1.54 ± 0.16 R$_\oplus$ although we remind the reader that the exact value is dependent on the planet's separation (see Fig. 11). A consistent value of $1.55^{+0.52}_{-0.50}$ is also recovered, albeit with reduced signficance, around stars later than about M2.5V. This value is slightly lower than the valley locations measured around Sun-like stars with $M_s \sim 1.2$ M$_\odot$ of ~ 1.9 R$_\oplus$ and $M_s \sim 0.85$ M$_\odot$ of ~ 1.7 R$_\oplus$ (Fulton & Petigura 2018).

7.3. Imperfect clearing of the radius valley

As evidenced in Fig. 8, the radius valley around low mass stars is partially filled by planets. This feature

This work elucidates the location of the radius valley around M dwarf host stars and guides observers to the planetary radii from transit surveys that are of interest for fully characterizing the radius valley in terms of planetary bulk densities.

mass dependence of the gap:

The weighted feature radii are also effected by planetary magnetic fields which directly impact the efficiency of atmospheric stripping in the photoevaporation scenario (**?**). The persistence of a planetary magnetic field acts to shield the planet's atmosphere from XUV stellar photons thus enhancing the retention of the atmosphere and shifting the location of the radius valley to larger radii.

valley filling increases with deacreasing stellar mass

In the photoevaporation scenario, the partial filling of the gap around low mass stars may be explained by their lower XUV luminosities relative to Sun-like such as those included in the CKS stellar sample ().

This explanation seems to be supported by the stellar mass dependent gap measurements from Fulton & Petigura (2018).

summary of McDonald+2019 (https://ui-adsabs-harvard-edu.ezp-prod1.hul.harvard.edu/abs/2019ApJ...876...22M/abstract): X-rays only since XUV observations are difficult for non-Sun-like stars and X-rays are the dominant driver of atmospheric loss by photoevaporation. Jackson+12 & Shkolnik+14 derived scalings from data for the LX/Lbol evolution over time for 0.3 - 1.3 solar mass stars on the MS, low mass stars ($\lesssim 0.8$ M$_\odot$) exhibit a LX/Lbol that is typically a few to ten times greater than around Sun-like stars ($0.8 - 1.12$ M$_\odot$) (fig 1 in McDonald+2019). scaling these values by the typical bolometric luminosities of stars in the various mass bins reveals that Sun-like stars having higher absolute X-ray

luminosities which contributes to more efficient clearing of the gap by photoevaporation.

REFERENCES

Aigrain, S., Hodgkin, S. T., Irwin, M. J., Lewis, J. R., & Roberts, S. J. 2015, MNRAS, 447, 2880

Aigrain, S., Parviainen, H., & Pope, B. J. S. 2016, MNRAS, 459, 2408

Akeson, R. L., Chen, X., Ciardi, D., et al. 2013, PASP, 125, 989

Bailer-Jones, C. A. L., Rybizki, J., Fouesneau, M., Mantelet, G., & Andrae, R. 2018, AJ, 156, 58

Barclay, T., Pepper, J., & Quintana, E. V. 2018, ArXiv e-prints, arXiv:1804.05050

Barnes, J. W. 2007, PASP, 119, 986

Barnes, R., & Greenberg, R. 2006, ApJL, 647, L163

Berger, T. A., Huber, D., Gaidos, E., & van Saders, J. L. 2018, ApJ, 866, 99

Bouchy, F., Doyon, R., Artigau, É., et al. 2017, The Messenger, 169, 21

Bovy, J., Rix, H.-W., Green, G. M., Schlafly, E. F., & Finkbeiner, D. P. 2016, ApJ, 818, 130

Boyajian, T. S., von Braun, K., van Belle, G., et al. 2012, ApJ, 757, 112

Burke, C. J., & Catanzarite, J. 2017, Planet Detection Metrics: Per-Target Flux-Level Transit Injection Tests of TPS for Data Release 25, Tech. rep.

Burke, C. J., Christiansen, J. L., Mullally, F., et al. 2015, ApJ, 809, 8

Chen, H., & Rogers, L. A. 2016, ApJ, 831, 180

Chen, J., & Kipping, D. 2017, ApJ, 834, 17

Choi, J., Dotter, A., Conroy, C., et al. 2016, ApJ, 823, 102

Christiansen, J. L., Clarke, B. D., Burke, C. J., et al. 2015, ApJ, 810, 95

—. 2016, ApJ, 828, 99

Christiansen, J. L., Vanderburg, A., Burt, J., et al. 2017, AJ, 154, 122

Claret, A., Hauschildt, P. H., & Witte, S. 2012, A&A, 546, A14

Cloutier, R. 2019, AJ, 158, 81

Crossfield, I. J. M., Ciardi, D. R., Petigura, E. A., et al. 2016, ApJS, 226, 7

Donati, J.-F., Kouach, D., Lacombe, M., et al. 2018, SPIRou: A NIR Spectropolarimeter/High-Precision Velocimeter for the CFHT, 107

Dressing, C. D., & Charbonneau, D. 2013, ApJ, 767, 95

—. 2015, ApJ, 807, 45

Dressing, C. D., Charbonneau, D., Dumusque, X., et al. 2015, ApJ, 800, 135

Dressing, C. D., Vanderburg, A., Schlieder, J. E., et al. 2017, AJ, 154, 207

Eker, Z., Bakış, V., Bilir, S., et al. 2018, MNRAS, 479, 5491

Fressin, F., Torres, G., Charbonneau, D., et al. 2013, ApJ, 766, 81

Fulton, B. J., & Petigura, E. A. 2018, AJ, 156, 264

Fulton, B. J., Petigura, E. A., Howard, A. W., et al. 2017, AJ, 154, 109

Gaidos, E., Mann, A. W., Kraus, A. L., & Ireland, M. 2016, MNRAS, 457, 2877

Ginzburg, S., Schlichting, H. E., & Sari, R. 2018, MNRAS, 476, 759

Gupta, A., & Schlichting, H. E. 2019a, MNRAS, 487, 24

—. 2019b, arXiv e-prints, arXiv:1907.03732

Hardegree-Ullman, K. K., Cushing, M. C., Muirhead, P. S., & Christiansen, J. L. 2019, AJ, 158, 75

Henry, T. J., & McCarthy, Jr., D. W. 1993, AJ, 106, 773

Hirano, T., Dai, F., Gandolfi, D., et al. 2018, AJ, 155, 127

Howard, A. W., Marcy, G. W., Bryson, S. T., et al. 2012, ApJS, 201, 15

Howell, S. B., Sobeck, C., Haas, M., et al. 2014, PASP, 126, 398

Huber, D., Zinn, J., Bojsen-Hansen, M., et al. 2017, ApJ, 844, 102

Jenkins, J. M., Chandrasekaran, H., McCauliff, S. D., et al. 2010, in SPIE, Vol. 7740, Software and Cyberinfrastructure for Astronomy, 77400D

Jenkins, J. M., Twicken, J. D., McCauliff, S., et al. 2016, in SPIE, Vol. 9913, Software and Cyberinfrastructure for Astronomy IV, 99133E

Jin, S., & Mordasini, C. 2018, ApJ, 853, 163

Jin, S., Mordasini, C., Parmentier, V., et al. 2014, ApJ, 795, 65

Kotani, T., Tamura, M., Suto, H., et al. 2014, in SPIE, Vol. 9147, Ground-based and Airborne Instrumentation for Astronomy V, 914714

Kreidberg, L. 2015, PASP, 127, 1161

Kruse, E., Agol, E., Luger, R., & Foreman-Mackey, D. 2019, ApJS, 244, 11

Lee, E. J., & Chiang, E. 2016, ApJ, 817, 90

Lee, E. J., Chiang, E., & Ormel, C. W. 2014, ApJ, 797, 95

Li, J., Tenenbaum, P., Twicken, J. D., et al. 2018, arXiv e-prints, arXiv:1812.00103

Lindegren, L., Hernández, J., Bombrun, A., et al. 2018, A&A, 616, A2

Livingston, J. H., Crossfield, I. J. M., Petigura, E. A., et al. 2018, AJ, 156, 277

Lopez, E. D., & Fortney, J. J. 2014, ApJ, 792, 1

Lopez, E. D., & Rice, K. 2018, MNRAS, 479, 5303

Luger, R., Agol, E., Kruse, E., et al. 2016, AJ, 152, 100

Luger, R., Kruse, E., Foreman-Mackey, D., Agol, E., & Saunders, N. 2018, AJ, 156, 99

Lundkvist, M. S., Kjeldsen, H., Albrecht, S., et al. 2016, Nature Communications, 7, 11201

Mahadevan, S., Ramsey, L., Bender, C., et al. 2012, in SPIE, Vol. 8446, Ground-based and Airborne Instrumentation for Astronomy IV, 84461S

Mamajek, E. E., Torres, G., Prsa, A., et al. 2015, arXiv e-prints, arXiv:1510.06262

Mandel, K., & Agol, E. 2002, ApJL, 580, L171

Mann, A. W., Feiden, G. A., Gaidos, E., Boyajian, T., & von Braun, K. 2015, ApJ, 804, 64

Martinez, C. F., Cunha, K., Ghezzi, L., & Smith, V. V. 2019, ApJ, 875, 29

Mathur, S., Huber, D., Batalha, N. M., et al. 2017, ApJS, 229, 30

Mayo, A. W., Vanderburg, A., Latham, D. W., et al. 2018, AJ, 155, 136

Mazeh, T., Holczer, T., & Faigler, S. 2016, A&A, 589, A75

Montet, B. T., Morton, T. D., Foreman-Mackey, D., et al. 2015, ApJ, 809, 25

Morton, T. D. 2012, ApJ, 761, 6

—. 2015, VESPA: False positive probabilities calculator, Astrophysics Source Code Library, ascl:1503.011

Morton, T. D., & Swift, J. 2014, ApJ, 791, 10

Owen, J. E., & Wu, Y. 2013, ApJ, 775, 105

—. 2017, ApJ, 847, 29

Pecaut, M. J., & Mamajek, E. E. 2013, ApJs, 208, 9

Petigura, E. A., Howard, A. W., & Marcy, G. W. 2013, Proceedings of the National Academy of Science, 110, 19273

Petigura, E. A., Howard, A. W., Marcy, G. W., et al. 2017, AJ, 154, 107

Petigura, E. A., Marcy, G. W., Winn, J. N., et al. 2018, AJ, 155, 89

Quirrenbach, A., Amado, P. J., Caballero, J. A., et al. 2014, in SPIE, Vol. 9147, Ground-based and Airborne Instrumentation for Astronomy V, 91471F

Ricker, G. R., Winn, J. N., Vanderspek, R., et al. 2015, Journal of Astronomical Telescopes, Instruments, and Systems, 1, 014003

Rogers, L. A. 2015, ApJ, 801, 41

Stassun, K. G., Oelkers, R. J., Paegert, M., et al. 2019, AJ, 158, 138

Twicken, J. D., Catanzarite, J. H., Clarke, B. D., et al. 2018, Publications of the Astronomical Society of the Pacific, 130, 064502

Van Eylen, V., Agentoft, C., Lundkvist, M. S., et al. 2018, MNRAS, 479, 4786

Vanderburg, A., & Johnson, J. A. 2014, PASP, 126, 948

Weiss, L. M., & Marcy, G. W. 2014, ApJL, 783, L6

Wu, Y. 2019, ApJ, 874, 91

Youdin, A. N. 2011, ApJ, 742, 38

Zhu, W., Petrovich, C., Wu, Y., Dong, S., & Xie, J. 2018, ApJ, 860, 101